# Design of metal-dielectric grating lasers only supporting surface-wave-like modes

**Po-Jui Chiang**[1] **and Shu-Wei Chang**[2,3,*]

[1]*Department of Electronic Engineering, National Kaohsiung University of Applied Sciences, Kaohsiung 80778, Taiwan*
[2]*Research Center for Applied Sciences, Academia Sinica, Nankang, Taipei 11529, Taiwan*
[3]*Department of Photonics, National Chiao-Tung University, Hsinchu 30010, Taiwan*
**swchang@sinica.edu.tw*

**Abstract:** We present a prototype of semiconductor lasers with plasmonic periodic structures that only support transverse-magnetic modes at telecommunication wavelengths. The structure does not sustain transverse-electric guided modes which are irrelevant to surface-wave-enhanced applications, and lasing modes must be surface-wave-like. With thin low-index dielectric buffers near the metal surface, the threshold gain is kept at a decent level around the photonic band edge. Thin windows are then opened on the metal surface to let out significant surface fields. This facilitates usages of surface waves for the spectroscopy and sensing.

**OCIS codes:** (050.1755) Computational electromagnetic methods; (130.5296) Photonic crystal waveguides; (250.5403) Plasmonics

---

## References and links

1. H. Raether, *Surface Plasmons on Smooth and Rough Surfaces and on Gratings*, Springer Tracts in Modern Physics, vol. 111 (Springer, 1988).
2. U. Kreibig and M. Vollmer, *Optical Properties of Metal Clusters*, Springer Series in Materials Science, vol. 25 (Springer, 1995).
3. M. I. Stockman, *Electromagnetic Theory of SERS*, Surface-Enhanced Raman Scattering, Topics in Applied Physics, vol. 103 (Springer Berlin, 2006). pp. 47-65.
4. J. Homola, S. S. Yee, and G. Gauglitzb, “Surface plasmon resonance sensors: review,” Sensors and Actuators B: Chemical **54**, 3–15 (1999).
5. T. Liebermann and W. Knoll, “Surface-plasmon field-enhanced fluorescence spectroscopy,” Colloid. Surface A **171**, 115–130 (2000).
6. W. L. Barnes, A. Dereux, and T. W. Ebbesen, “Surface plasmon subwavelength optics,” Nature **424**, 824–830 (2003).
7. A. V. Zayats, I. I. Smolyaninovb, and A. A. Maradudinc, “Nano-optics of surface plasmon polaritons,” Phys. Rep. **408**, 131–314 (2005).
8. C. J. Orendorff, A. Gole, T. K. Sau, and C. J. Murphy, “Surface-enhanced Raman spectroscopy of self-assembled monolayers: sandwich architecture and nanoparticle shape dependence,” Anal. Chem. **77**, 3261–3266 (2005).
9. C. E. Talley, J. B. Jackson, C. Oubre, N. K. Grady, C. W. Hollars, S. M. Lane, T. R. Huser, P. Nordlander, and N. J. Halas, “Surface-enhanced Raman scattering from individual Au nanoparticles and nanoparticle dimer substrates,” Nano. Lett. **5**, 1569–1574 (2005).
10. G. Nemova and R. Kashyap, “Fiber-bragg-grating-assisted surface plasmon-polariton sensor,” Opt. Lett. **31**, 2118–2120 (2006).
11. L. Pang, G. M. Hwang, B. Slutsky, and Y. Fainman, “Spectral sensitivity of two-dimensional nanohole array surface plasmon polariton resonance sensor,” Appl. Phys. Lett. **91**, 123112 (2007).
12. K. A. Willets and R. P. Van Duyne, “Localized surface plasmon resonance spectroscopy and sensing,” Annu. Rev. Phys. Chem. **58**, 267–297 (2007).
13. A. V. Kabashin, P. Evans, S. Pastkovsky, W. Hendren, G. A. Wurtz, R. Atkinson, R. Pollard, V. A. Podolskiy, and A. V. Zayats, “Plasmonic nanorod metamaterials for biosensing,” Nat. Mater **8**, 867–871 (2009).

#222834 - $15.00 USD Received 11 Sep 2014; revised 23 Oct 2014; accepted 27 Oct 2014; published 3 Nov 2014

14. L. Wu, H. S. Chu, W. S. Koh, and E. P. Li, “Highly sensitive graphene biosensors based on surface plasmon resonance,” Opt. Express **18**, 14395–14400 (2010).
15. M. T. Hill, Y. S. Oei, B. Smalbrugge, Y. Zhu, T. de Vries, P. J. van Veldhoven, F. W. M. van Otten, T. J. Eijkemans, J. P. Turkiewicz, H. de Waardt, E. J. Geluk, S. H. Kwon, Y. H. Lee, R. Notzel, and M. K. Smit, “Lasing in metallic-coated nanocavities,” Nat. Photonics **1**, 589–594 (2007).
16. M. T. Hill, M. Marell, E. S. P. Leong, B. Smalbrugge, Y. Zhu, M. Sun, P. J. van Veldhoven, E. J. Geluk, F. Karouta, Y.-S. Oei, R. Nötzel, C.-Z. Ning, and M. K. Smit, “Lasing in metal-insulator-metal sub-wavelength plasmonic waveguides,” Opt. Express **17**, 11107–11112 (2009).
17. M. J. Marell, B. Smalbrugge, E. J. Geluk, P. J. van Veldhoven, B. Barcones, B. Koopmans, R. Nötzel, M. K. Smit, and M. T. Hill, “Plasmonic distributed feedback lasers at telecommunications wavelengths,” Opt. Express **19**, 15109–15118 (2011).
18. K. Ding, Z. C. Liu, L. J. Yin, M. T. Hill, M. J. H. Marell, P. J. van Veldhoven, R. Nöetzel, and C. Z. Ning, “Room-temperature continuous wave lasing in deep-subwavelength metallic cavities under electrical injection,” Phys. Rev. B **85**, 041301 (2012).
19. K. Ding and C. Z. Ning, “Metallic subwavelength-cavity semiconductor nanolasers,” Light: Science and Applications **1**, e20 (2012).
20. A. Bousseksou, R. Colombelli, A. Babuty, Y. D. Wilde, Y. Chassagneux, C. Sirtori, G. Patriarche, G. Beaudoin, and I. Sagnes, “A semiconductor laser device for the generation of surface-plasmons upon electrical injection,” Opt. Express **17**, 9391–9400 (2009).
21. R. A. Flynn, C. S. Kim, I. Vurgaftman, M. Kim, J. R. Meyer, A. J. Mäkinen, K. Bussmann, L. Cheng, F.-S. Choa, and J. P. Long, “A room-temperature semiconductor spaser operating near 1.5 $\mu$m,” Opt. Express **19**, 8954–8961 (2011).
22. Y. Li, H. Zhang, N. Zhu, T. Mei, D. H. Zhang, and J. Teng, “Short-range surface plasmon propagation supported by stimulated amplification using electrical injection,” Opt. Express **19**, 22107–22112 (2011).
23. D. Y. Fedyanin, A. V. Krasavin, A. V. Arsenin, and A. V. Zayats, “Surface plasmon polariton amplification upon electrical injection in highly integrated plasmonic circuits,” Nano Lett. **12**, 2459–2463 (2012).
24. D. Costantini, A. Bousseksou, M. Fevrier, B. Dagens, and R. Colombelli, “Loss and gain measurements of tensile-strained quantum well diode lasers for plasmonic devices at telecom wavelengths,” IEEE J. Quantum Electron **48**, 73–78 (2012).
25. D. Costantini, L. Greusard, A. Bousseksou, R. Rungsawang, T. P. Zhang, S. Callard, J. Decobert, F. Lelarge, G.-H. Duan, Y. De Wilde, and R. Colombelli, “In situ generation of surface plasmon polaritons using a near-infrared laser diode,” Nano Lett. **12**, 4693–4697 (2012).
26. D. Costantini, L. Greusard, A. Bousseksou, Y. De Wilde, B. Habert, F. Marquier, J.-J. Greffet, F. Lelarge, J. Decobert, G.-H. Duan, and R. Colombelli, “A hybrid plasmonic semiconductor laser,” Appl. Phys. Lett. **102**, 101106 (2013).
27. A. Mizrahi, V. Lomakin, B. A. Slutsky, M. P. Nezhad, L. Feng, and Y. Fainman, “Low threshold gain metal coated laser nanoresonators,” Opt. Lett. **33**, 1261–1263 (2008).
28. Q. Ding, A. Mizrahi, Y. Fainman, and V. Lomakin, “Dielectric shielded nanoscale patch laser resonators,” Opt. Lett. **36**, 1812–1814 (2011).
29. W.-C. Liu, “High sensitivity of surface plasmon of weakly-distorted metallic surfaces,” Opt. Express **13**, 9766–9773 (2005).
30. M. L. Nesterov, A. V. Kats, and S. K. Turitsyn, “Extremely short-length surface plasmon resonance devices,” Opt. Express **16**, 20227–20240 (2008).
31. P. Berini and I. De Leon, “Surface plasmon-polariton amplifiers and lasers,” Nat. Photonics **6**, 16–24 (2012).
32. S. J. Al-Bader and M. Imtaar, “Optical fiber hybrid-surface plasmon polaritons,” J. Opt. Soc. Am. B **10**, 83–88 (1993).
33. Y.-C. Lu, L. Yang, W.-P. Huang, and S.-S. Jian, “Improved full-vector finite-difference complex mode solver for optical waveguides of circular symmetry,” J. Lightwave Technol. **26**, 1868–1876 (2008).
34. P.-J. Chiang and S. W. Chang, “Frequency-domain formulation of photonic crystals using sources and gain,” Opt. Express **21**, 1972–1985 (2013).
35. S. W. Chang, “Full frequency-domain approach to reciprocal microlasers and nanolasers–perspective from Lorentz reciprocity,” Opt. Express **19**, 21116–21134 (2011).
36. P.-J. Chiang, C.-L. Wu, C.-H. Teng, C.-S. Yang, and H.-C. Chang, “Full-vectorial optical waveguide mode solvers using multidomain pseudospectral frequency-domain (PSFD) formulations,” IEEE J. Quantum Electron **44**, 56–66 (2008).
37. P.-J. Chiang and Y.-C. Chiang, “Pseudospectral frequency-domain formulae based on modified perfectly matched layers for calculating both guided and leaky modes,” IEEE Photon. Technol. Lett. **22**, 908–910 (2010).
38. T. Okamoto, J. Simonen, and S. Kawata, “Plasmonic band gaps of structured metallic thin films evaluated for a surface plasmon laser using the coupled-wave approach,” Phys. Rev. B **77**, 115425 (2008).
39. T. Okamoto and S. Kawata, “Dispersion relation and radiation properties of plasmonic crystals with triangular lattices,” Opt. Express **20**, 5168–5177 (2012).
40. L. Li, J. Chandezon, G. Granet, and J.-P. Plumey, “Rigorous and efficient grating-analysis method made easy for

Received 11 Sep 2014; revised 23 Oct 2014; accepted 27 Oct 2014; published 3 Nov 2014

optical engineers," Appl. Opt. **38**, 304–313 (1999).

41. M. Neviere and E. Popov, *Light Propagation in Periodic Media: Differential Theory and Design*, Optical Science and Engineering (CRC Press, 2002).
42. T. Visser, H. Blok, B. Demeulenaere, and D. Lenstra, "Confinement factors and gain in optical amplifiers," IEEE J. Quantum Electron **33**, 1763–1766 (1997).
43. A. V. Maslov and C.-Z. Ning, "Modal gain in a semiconductor nanowire laser with anisotropic bandstructure," IEEE J. Quantum Electron **40**, 1389–1397 (2004).
44. S. W. Chang and S. L. Chuang, "Fundamental formulation for plasmonic nanolasers," IEEE J. Quantum Electron **45**, 1014–1023 (2009).
45. T. W. Nee and A. K. Green, "Optical properties of InGaAs lattice-matched to InP," J. Appl. Phys. **68**, 5314–5317 (1990).
46. E. D. Palik, ed., *Handbook of Optical Constants of Solids* (Academic, 1985).
47. P. B. Johnson and R. W. Christy, "Optical constants of the noble metals," Phys. Rev. B **6**, 4370–4379 (1972).
48. C.-Y. Lu, S. W. Chang, S. L. Chuang, T. D. Germann, U. W. Pohl, and D. Bimberg, "Low thermal impedance of substrate-free metal cavity surface-emitting microlasers," IEEE Photon Technol. Lett. **23**, 1031–1033 (2011).

---

## 1. Introduction

Surface plasmon polaritons (SPPs) have been employed in various areas [1–3]. The intense fields of SPP modes at interfaces of metals and dielectrics make many applications that require a high intensity accessible. This feature also enhances the resolution and sensitivity which are essential for the spectroscopy and sensing [4–14]. Recently, SPP modes have also been utilized in electrically-injected semiconductor lasers (SLs) and amplifiers [15–26]. These active nanophotonic devices provide the advanced probing capability and functionality. Integrating them with present schemes of the surface-wave-enhanced (SW-enhanced) spectroscopy and sensing may further compact measurement setups and increase the signal-to-noise ratio.

Despite demonstrations and developments of plasmonic SLs and amplifiers with planar or metal-grating structures [20–26], a few obstacles remain to be solved. The most critical one is the loss. Due to lossy metals and high fields near dielectric-metal interfaces, propagation distances of transverse-magnetic-like (TM-like) SPP modes are usually limited. One remedy to this problem is the inclusion of other photonic structures, for example, dielectric layers [27,28], as buffers which reduce the metal loss but still preserve the characteristics of SPP waves. Yet, SPP modes are often not the only modes in photonic structures. For instance, transverse-electric-like (TE-like) guided modes may be present. These modes lack significant surface fields that enhance interactions near surfaces. In addition, unless TE-like modes are (nearly) cut off, their lasing thresholds are often lower than those of SPP modes [16, 19]. If a photonic structure supports both the TE-like and TM-like SPP modes, usually TE-like ones dominate in the presence of gain, which is not useful in SW-enhanced applications. To favor SPP modes in these conditions, specific semiconductor nanostructures such as tensile-strained multiple quantum wells which provide the higher TM than TE gains have to be used [24–26]. Another issue on SPP modes is their sensitivity to corrugated metal surfaces and guiding structures [29, 30]. Precise fabrications are required in these cases.

In this work, we present the design of an electrically-injected SL structure which contains a metal-dielectric grating and merely supports SPP-like modes for SW-enhanced applications. Since no TE-like modes are supported, the active medium could simply be a bulk semiconductor that provides the isotropic rather than TM gain at telecommunication wavelengths. We manage the metal loss with a low-index dielectric grating which confines the field and reduces its penetration into the metal [27,28]. The attainable gain of bulk semiconductors is estimated to ensure that it could surpass the propagation loss of SPP modes. The current paths are reserved between dielectric buffers of the grating so that the electrical injection is possible. A significant surface field for SW-enhanced applications is then let out at windows opened on metal surfaces. Since only SPP-like modes are supported in this structure, TE-like modes that are irrelevant for

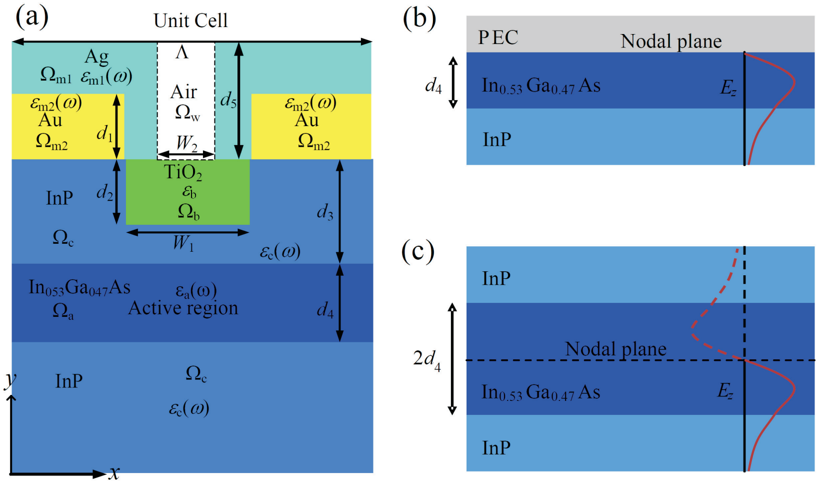

Fig. 1. (a) The schematic diagram of a unit cell in the laser cavity. The active region, dielectric buffer, WG cladding, and two metal regions are denoted as $\Omega_a$, $\Omega_b$, $\Omega_c$, and $\Omega_{m,1(2)}$, respectively. A window ($\Omega_w$, dashed-line region) at the center of Ag covering will be opened to let out the surface field. (b) The limiting case at $d_3 = 0$. The metal is approximated as a PEC. The electric fields of TE modes vanish on the nodal plane. (c) The corresponding TE modes in a symmetric WG twice wider in the core. They are odd TE modes of the symmetric WG and all have finite cutoff frequencies.

SW-enhanced applications would not dominate in lasing fields.

The remaining part of the paper is organized as follows. The structure of metal-dielectric grating lasers is described in section 2. The basic formulation and some physical parameters that help design the laser structure are briefly introduced in section 3. In section 4, we present the designs and calculations of the grating laser structure. A conclusion is given in section 5.

## 2. Semiconductor laser structure with metal-dielectric grating

There are various structures of plasmonic lasers and amplifiers [31]. Here, we adopt a grating structure whose unit cell is shown in Fig. 1(a). For realistic fabrications, the structure could be further modified.

The grating has a period $\Lambda$. It is based on semiconductors indium phosphide (InP) and indium gallium arsenide (In$_{0.53}$Ga$_{0.47}$As) lattice-matched to InP, both of which are III-V materials commonly used at telecommunication wavelengths. Semiconductor InP functions as the upper and lower waveguide (WG) claddings (region $\Omega_c$), and In$_{0.53}$Ga$_{0.47}$As acts as the WG core and gain material ($\Omega_a$). A periodic pattern of dielectric buffers ($\Omega_b$) composed of titanium dioxide (TiO$_2$) is introduced into the upper InP layer. The intervening regions of InP between dielectric buffers function as current paths and are covered with gold (Au), which is utilized as ohmic contacts to avoid the Schottky barrier for injected carriers. The whole structure is then deposited with silver (Ag). The regions of Ag and Au are denoted as $\Omega_{m,1}$ and $\Omega_{m,2}$, respectively. The two metals act as plasma materials, and together with TiO$_2$, they form a metal-dielectric grating. The thickness and width of each dielectric buffer in the grating affect field strengths of TM-like modes penetrating into metals [27, 28]. Therefore, the sizes of dielectric chunks could be utilized to control the loss. On the other hand, most of the lasing field is blocked by the Ag covering and cannot reach the surface for spectroscopic and sensing applications. Therefore, after the loss is reduced to an acceptable level, a narrow window ($\Omega_w$) will be opened at the center of Ag covering to let out the surface field.

The triple layers of InP/In$_{0.53}$Ga$_{0.47}$As/InP form a natural slab WG due to the high refractive index of In$_{0.53}$Ga$_{0.47}$As. Therefore, the SPP-like modes in this grating structure exhibit both features of guided TM modes from the slab WG and surface waves at interfaces of the metal and dielectric, namely, a hybrid mode. Once carriers are injected into the active region of In$_{0.53}$Ga$_{0.47}$As, the hybrid mode experiences the gain there and compensates the ohmic loss near the metal-dielectric interface. The thickness $d_3$ of the upper InP layer could be designed (several tens of nanometers) so that fields of SPP-like hybrid modes are mostly confined near the metal-dielectric interface rather than in the WG core [32,33]. In this way, the spatially sharp surface field is preserved in this grating structure.

The TE-like guided modes are absent if the In$_{0.53}$Ga$_{0.47}$As and upper InP layers are sufficiently thin and hence cut off these modes. The cutoff of TE-like guided modes could be expected if one considers the limiting case in which the upper InP layer is absent ($d_3 = 0$), and metal is approximated as a perfect electric conductor (PEC). Under such circumstances, the metal-semiconductor layer structure turns into an asymmetric slab WG shown in Fig. 1(b). The electric fields $E_z(y)$ of TE modes in this asymmetric WG have to vanish at the PEC interface. From the image theory of electromagnetism, these modes are linked to the odd TE$_m$ modes ($m = 1,3...$) of a symmetric slab WG twice wider in the core ($2d_4$), as indicated in Fig. 1(c). It is known that odd TE modes in a symmetric slab WG are all cut off if the core is thin enough. Equivalently, if the core thickness $d_4$ of the asymmetric WG is sufficiently thin, each guided TE mode in this limiting case disappears. Note that the fundamental TM mode of the asymmetric WG is not constrained by the PEC boundary and hence is not cut off. While the aforementioned scenario is true in the limiting case, it should remain valid if (1) thicknesses $d_3$ and $d_4$ are sufficiently small, and (2) the refractive index of the dielectric grating is decently but not too much lower than that of InP. Condition (2) could further shorten the effective optical length of the upper cladding normal to the planar structure before the index guiding in semiconductor layers due to the low-index dielectric comes into play. Numerical calculations indicate that TE guided modes can be indeed eliminated in this way.

## 3. Basic formulation

We employ a frequency-domain method which incorporates sources (gain) into optical modes of periodic photonic structures [34,35]. In this approach, Maxwell's equations in the presence of sources (gain) is converted to a generalized eigenvalue (GE) problem for Bloch modes. A multidomain pseudospectral frequency-domain method is also numerically realized in the approach to enhance the convergence [36,37]. Since sources (gain) are built into the formulation, we can directly look into the issues of loss, threshold gain, and their structural dependencies, which are often inferred indirectly in other approaches [38–41].

For the grating in Fig. 1(a), let us consider a source-driven Bloch mode $\mathbf{f}_{n,k_x}(\boldsymbol{\rho},\omega)$ ($\boldsymbol{\rho} = x\hat{x} + y\hat{y}$) labeled with a band index $n$, wave number $k_x$ along the direction of periodicity, and real frequency $\omega$. The wave equation and boundary condition of $\mathbf{f}_{n,k_x}(\boldsymbol{\rho},\omega)$ are [34]

$$\nabla\times\nabla\times\mathbf{f}_{n,k_x}(\boldsymbol{\rho},\omega) - \left(\frac{\omega}{c}\right)^2 \varepsilon_{\mathrm{r}}(\boldsymbol{\rho},\omega)\mathbf{f}_{n,k_x}(\boldsymbol{\rho},\omega) = i\omega\mu_0\mathbf{j}_{\mathrm{s},n,k_x}(\boldsymbol{\rho},\omega), \tag{1a}$$

$$\mathbf{j}_{\mathrm{s},n,k_x}(\boldsymbol{\rho},\omega) = -i\omega\varepsilon_0\Delta\varepsilon_{\mathrm{r},n,k_x}(\omega)U(\boldsymbol{\rho})\mathbf{f}_{n,k_x}(\boldsymbol{\rho},\omega), \tag{1b}$$

$$\mathbf{f}_{n,k_x}(\boldsymbol{\rho}+\Lambda\hat{x},\omega) = e^{ik_x\Lambda}\mathbf{f}_{n,k_x}(\boldsymbol{\rho},\omega), \tag{1c}$$

where $\varepsilon_0$, $\mu_0$, and $c$ are permittivity, permeability, and speed of light in the vacuum; $\varepsilon_{\mathrm{r}}(\boldsymbol{\rho},\omega)$ is the periodic relative permittivity distribution of the grating structure; $\mathbf{j}_{\mathrm{s},n,k_x}(\boldsymbol{\rho},\omega)$ is the associated source which generates the mode; $U(\boldsymbol{\rho})$ is an indicator function which is unity in

#222834 - $15.00 USD Received 11 Sep 2014; revised 23 Oct 2014; accepted 27 Oct 2014; published 3 Nov 2014

the active region $\Omega_{\mathrm{a}}$ but zero elsewhere; and $\Delta\varepsilon_{\mathrm{r},n,k_x}(\omega)$ is a proportional factor which derives its dependence on $\omega$ through numerical calculations. The relative permittivity $\varepsilon_{\mathrm{r}}(\boldsymbol{\rho},\omega)$ is locally homogeneous and equal to $\varepsilon_u(\omega)$ in region $\Omega_u$ ($u = \mathrm{a,b,c,m_1,m_2,w}$). From Eq. (1b), $\mathbf{j}_{\mathrm{s},n,k_x}(\boldsymbol{\rho},\omega)$ is only present in the active region $\Omega_{\mathrm{a}}$ and proportional to mode profile $\mathbf{f}_{n,k_x}(\boldsymbol{\rho},\omega)$. If we substitute this expression into Eq. (1a), the wave equation becomes a GE problem of $\mathbf{f}_{n,k_x}(\boldsymbol{\rho},\omega)$ with $\Delta\varepsilon_{\mathrm{r},n,k_x}(\omega)$ acting as the eigenvalue. Once $\Delta\varepsilon_{\mathrm{r},n,k_x}(\omega)$ is obtained, it could be combined with the permittivity $\varepsilon_{\mathrm{a}}(\omega)$ of the gain material and interpreted as the amount of permittivity variation which makes the mode self oscillate at frequency $\omega$ [34,35].

In region $u$, we simplify the GE problem with the operator identity $\nabla\times\nabla\times = \nabla(\nabla\cdot) - \nabla^2$ in the cartesian coordinate and null-divergence condition. This simplification is allowed because the field is present in a seemingly charge-free domain with an effective homogeneous permittivity $\varepsilon_u(\omega)+\delta_{u\mathrm{a}}\Delta\varepsilon_{\mathrm{r},n,k_x}(\omega)$, where $\delta_{u\mathrm{a}}$ is the Kronecker delta. Boundary conditions of various field components are utilized to connect fields in different regions together. In this way, the GE problem in region $u$ is rewritten in terms of Hemholtz equation as

$$-\left(\frac{\partial^2}{\partial x^2}+\frac{\partial^2}{\partial y^2}\right)\mathbf{f}_{n,k_x}(\boldsymbol{\rho},\omega)-\left(\frac{\omega}{c}\right)^2\varepsilon_u(\omega)\mathbf{f}_{n,k_x}(\boldsymbol{\rho},\omega)=\delta_{u\mathrm{a}}\left(\frac{\omega}{c}\right)^2\Delta\varepsilon_{\mathrm{r},n,k_x}(\omega)\mathbf{f}_{n,k_x}(\boldsymbol{\rho},\omega). \quad (2)$$

Perfectly matched layers [37] are then imposed on the top and bottom of computation domains to absorb outgoing waves along $\pm\hat{y}$ directions in cases of leaky modes.

Some useful parameters utilized in designs of the grating structure were derived in previous works [34, 35]. Dispersion relations of Bloch modes ($\omega_{n,k_x}$) are obtained by finding the frequency that minimizes the absolute value $|\omega\Delta\varepsilon_{\mathrm{r},n,k_x}(\omega)|$ at a given wave number $k_x$. With the frequency $\omega_{n,k_x}$ and cold-cavity condition (no gain or absorption from interband transitions is included in $\mathrm{Im}[\varepsilon_{\mathrm{a}}(\omega)]$ of the gain material), we estimate the threshold gain $g'_{\mathrm{th},n,k_x}$ of mode $(n,k_x)$ without the mirror loss at output facets as follows [35]:

$$g'_{\mathrm{th},n,k_x} = -2\left(\frac{\omega}{c}\right)\mathrm{Im}\left[\sqrt{\varepsilon_{\mathrm{a}}(\omega)+\Delta\varepsilon_{\mathrm{r},n,k_x}(\omega)}-\sqrt{\varepsilon_{\mathrm{a}}(\omega)}\right]\Bigg|_{\omega=\omega_{n,k_x}}. \quad (3)$$

If the contents of two square roots in Eq. (3) are dominated by the positive real part $\mathrm{Re}[\varepsilon_{\mathrm{a}}(\omega)]$, this threshold gain could be further approximated with binomial expansions as

$$g'_{\mathrm{th},n,k_x} \approx -\left(\frac{\omega}{c}\right)\frac{\mathrm{Im}[\Delta\varepsilon_{\mathrm{r},n,k_x}(\omega)]}{\sqrt{\mathrm{Re}[\varepsilon_{\mathrm{a}}(\omega)]}}\Bigg|_{\omega=\omega_{n,k_x}}. \quad (4)$$

For simplicity of designs and to obtain a rough picture of modal dispersions first, we would begin with the slab WG in absence of dielectric buffers and Au contacts, namely, $\mathrm{TiO_2}$ and Au are replaced with InP and Ag, respectively. The complex propagation constant $\beta_n(\omega)$ of mode $n$ in this slab WG and its modal loss $\alpha_{\mathrm{M},n}(\omega) = 2\mathrm{Im}[\beta_n(\omega)]$ is calculated as a function of frequency $\omega$ using the cold-cavity condition of $\mathrm{In_{0.53}Ga_{0.47}As}$. The transparency gain $g_{\mathrm{tr},n}(\omega)$ which exactly compensates the propagation loss can be estimated from $\alpha_{\mathrm{M},n}(\omega)$ as [42–44]

$$g_{\mathrm{tr},n}(\omega) \approx \frac{\alpha_{\mathrm{M},n}(\omega)}{\Gamma_{\mathrm{wg},n}(\omega)}, \qquad \Gamma_{\mathrm{wg},n}(\omega) = \frac{\frac{n_{\mathrm{a}}(\omega)}{2\eta_0}\int_{\Omega_{\mathrm{a}}}\mathrm{d}y|\mathbf{E}_n(y,\omega)|^2}{\int_{-\infty}^{\infty}\mathrm{d}y\frac{1}{2}\mathrm{Re}[\mathbf{E}_n(y,\omega)\times\mathbf{H}_n^*(y,\omega)]\cdot\hat{x}}, \quad (5)$$

where $\Gamma_{\mathrm{wg},n}(\omega)$ is the WG confinement factor; $n_{\mathrm{a}}(\omega)$ is the real part of the refractive index in the active region; $\eta_0$ is the intrinsic impedance; and $\mathbf{E}_n(y,\omega)$ and $\mathbf{H}_n(y,\omega)$ are the electric and magnetic fields of WG mode $n$. Equation (5) will be utilized to investigate dissipations and feasibilities of the slab WG and associated variations. The designs related to periodic dielectric buffers, Au contacts, and windows of surface fields are then considered afterward.

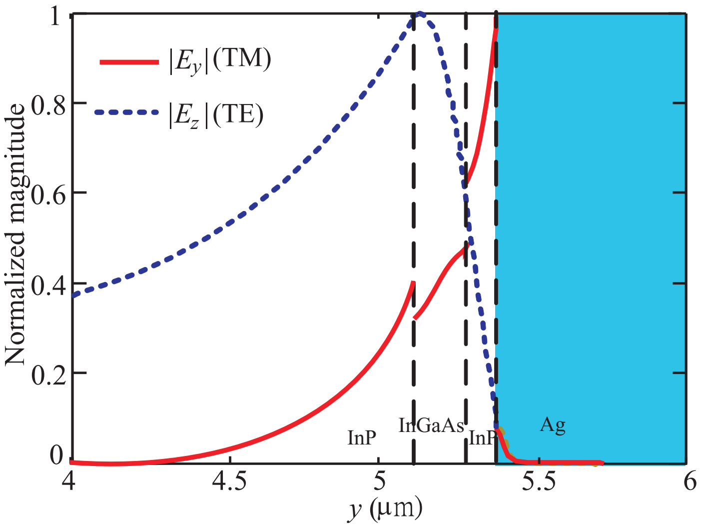

Fig. 2. Normalized magnitude profiles of the fundamental TM ($|E_y(y)|$) and TE ($|E_z(y)|$) modes at $\hbar\omega = 0.8$ eV. The TM mode peaks at the metal-semiconductor interface.

## 4. Calculations and discussions

In the calculations hereafter, we utilize the following data of material permittivities. The permittivities $\varepsilon_a(\omega)$ ($In_{0.53}Ga_{0.47}As$) and $\varepsilon_c(\omega)$ (InP) are adopted from Refs. [45] and [46], respectively. The two metal permittivities $\varepsilon_{m,1}(\omega)$ (Ag) and $\varepsilon_{m,2}(\omega)$ (Au) are obtained from Ref. [47]. The dielectric permittivity $\varepsilon_b(\omega)$ ($TiO_2$) is set to a nondispersive number 6.026.

### *4.1. Metal-semiconductor slab waveguide*

The metal-semiconductor slab WG is the precursor of the more complicated grating structure. We preliminarily set the thicknesses $d_3$ of upper InP layer, $d_4$ of $In_{0.53}Ga_{0.47}As$ layer, and $d_5$ of Ag covering to 0.19, 0.12, and 0.4 $\mu$m, respectively. The heights $d_1$ of Au contacts and $d_2$ of $TiO_2$ buffers are set to zero, and therefore the grating period virtually vanishes ($\Lambda = 0$).

The fundamental TE and TM modes are the only two guided modes in this WG around the telecommunication wavelength 1.55 $\mu$m. The fundamental TM mode is a SPP-like one. As shown in Fig. 2, its magnitude of the normalized field component $|E_y(y)|$ at a photon energy $\hbar\omega = 0.8$ eV (1.55 $\mu$m in wavelength, and $\hbar$ is Planck constant) has a sharp and maximal peak at InP side of the semiconductor-metal interface ($y = 5.32$ $\mu$m). In addition, the field component $E_y(y)$ is discontinuous at various material interfaces due to continuity of the displacement field $D_y(y)$ normal to the planar structure. On the other hand, the normalized magnitude $|E_z(y)|$ of the fundamental TE mode in the same figure indicates that it is guided by the $In_{0.53}Ga_{0.47}As$ WG core ($y = 5.13 - 5.25$ $\mu$m). The electric field of this TE mode is continuous. However, it penetrates into the InP substrate significantly and is not well confined in the active region.

Figure 3(a) shows the dispersion relations $\mathrm{Re}[\beta_n(\omega)]$ versus photon energy $\hbar\omega$ of the slab WG. Since the translational invariance of the WG structure can be regarded as a special case of vanishing periods, we may obtain analogous dispersion relations $k_x$ versus $\hbar\omega_{n,k_x}$ using the proposed GE approach with $\Lambda \to 0$. The results are also shown in Fig. 3(a) for comparisons. The two sets of dispersion curves agree well, which is also a validation of the GE method. The dispersion curve of the TE mode is close to the light line (dispersion curve of photons in three-dimensional plane-wave states) of InP. This explains why the TE mode profile in Fig. 2 has a

#222834 - $15.00 USD Received 11 Sep 2014; revised 23 Oct 2014; accepted 27 Oct 2014; published 3 Nov 2014

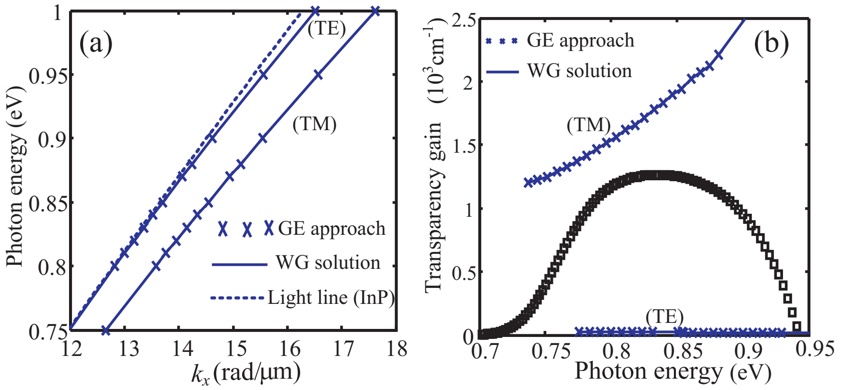

Fig. 3. (a) Dispersion relations of the fundamental TM and TE modes in the metal-semiconductor slab WG. The results from typical WG calculations and proposed GE approach agree well. The TE dispersion is close to the light line of InP (blue dashed line). (b) The transparency gains $g_{\text{tr},n}(\omega)$ as a function of $\hbar\omega$ for the same two modes. They match well with the curves $\hbar\omega_{n,k_x}$ versus $g'_{\text{th},n,k_x}$ from the GE approach. The material gain at $N = 4\times10^{18}$ cm$^{-3}$ is shown in black squares.

considerable distribution in the substrate.

Similarly, we may compare the transparency gain $g_{\text{tr},n}(\omega)$ as a function of $\hbar\omega$ with the threshold gain $g_{\text{th},n,k_x}$ parameterized by $\hbar\omega_{n,k_x}$ for the two modes. The two sets of curves are illustrated in Fig. 3(b), and they also match well with each other. As pointed out in section 1, TE-like modes often have much lower thresholds than those of TM-like ones in metallic photonic structures, and this metal-semiconductor WG is no exception. In the same figure, we also show the theoretical material gain spectrum of $\text{In}_{0.53}\text{Ga}_{0.47}\text{As}$ at a carrier density $N = 4\times10^{18}$ cm$^{-3}$, which is calculated using a Gaussian lineshape with a half-width-at-half-maximum linewidth of 22.5 meV. This carrier density is about 1.5 to 3 times higher than that in a conventional double-heterojunction SL and is chosen as a benchmark, presuming that the large gain necessary for loss compensations is achievable at a high injection level due to good thermal properties of metals [48]. From Fig. 3(b), even at this level of carrier density, the material gain is still lower than $g_{\text{tr},n}(\omega)$ of the fundamental TM mode but much higher than that of the poorly-guided TE mode on most of the gain spectrum. In fact, the material gain may support the propagation of the fundamental TE mode up to $\hbar\omega \approx 0.95$ eV. Under such circumstances, the TM SPP-like mode could hardly compete with the TE one.

To avoid the dominance of the fundamental TE mode in the presence of gain, we attempt to cut it off at $\hbar\omega = 0.95$ eV by varying the thickness $d_3$ of the upper InP cladding. Other length parameters remain the same. Once the TE guided mode at this photon energy is cut off, it would not exist in the gain window $\hbar\omega \in [0.7,\ 0.95]$ eV at the benchmark carrier density. In Fig. 4(a), we show effective indices $n_{\text{eff},n}(\omega) \equiv \text{Re}[\beta_n(\omega)]/k_0$ of the fundamental TM and TE modes as a function of $d_3$ at $\hbar\omega = 0.95$ eV, where $k_0 = \omega/c$ is the propagation constant in the vacuum. The cutoff takes place if the effective index is identical to the refractive index $n_\text{c}(\omega) = 3.202$ of InP at $\hbar\omega = 0.95$ eV. In that condition, the mode ceases being confined by the WG core and begins to leak into the InP substrate. From Fig. 4(a), the critical thickness $d_3$ at which the cuttoff occurs is around 0.1 $\mu$m. On the other hand, the effective index of the SPP-like TM mode increases as the thickness $d_3$ decreases, which is opposite to the behavior of the TE mode. In fact, the smaller thickness $d_3$ of the upper InP cladding makes the fundamental TM mode more surface-wave-like (SW-like). Meanwhile, the WG core is closer to the peak of the

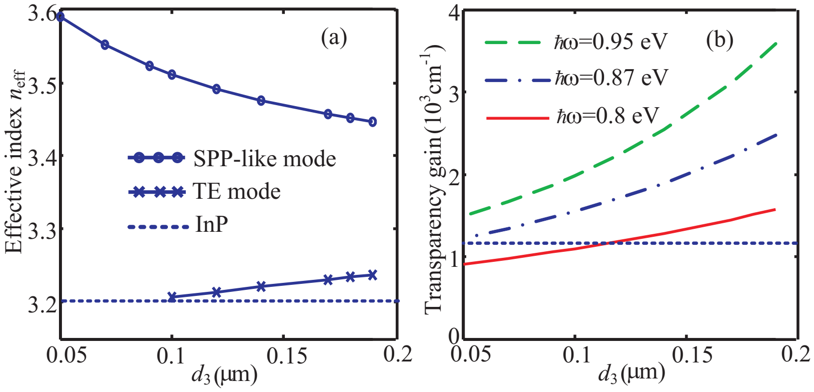

Fig. 4. (a) The effective indices $n_{\mathrm{eff},n}(\omega)$ of the fundamental TM and TE modes versus $d_3$ at $\hbar\omega = 0.95$ eV. The blue dashed line is the refractive index $n_{\mathrm{c}}(\omega) = 3.202$ of InP at the same photon energy. (b) The transparency gains $g_{\mathrm{tr},n}(\omega)$ of the SPP-like mode versus $d_3$ at $\hbar\omega = 0.8$, 0.87, and 0.95 eV. The material gain at $\hbar\omega = 0.8$ eV and $N = 4 \times 10^{18}$ cm$^{-3}$ is shown as the blue dashed line.

surface wave. This improves the mode confinement in the active region, and the transparency gain of the SPP-like mode is reduced, as shown in Fig. 4(b) for $g_{\mathrm{tr},n}(\omega)$ at $\hbar\omega = 0.8$, 0.87, and 0.95 eV in the gain window. The improvement of the lower-frequency mode is less significant even though the transparency gain at $\hbar\omega = 0.8$ eV could be slightly lower than the material gain at $d_3 \approx 0.115$ $\mu$m, as illustrated in the same figure.

As the thickness $d_3$ approaches zero, some portion of the transparency gain $g_{\mathrm{tr},n}(\omega)$ in the gain window at $\hbar\omega \in [0.7,\ 0.95]$ eV would be lower than the material gain. However, a finite thickness $d_3$ of the $n$-type InP cladding is necessary for proper current injections. A decent choice of $d_3$ is its critical value which just cuts off the fundamental TE mode at $\hbar\omega = 0.95$ eV, namely, $d_3 \approx 0.1$ $\mu$m. As can be inferred from Fig. 4(b), with this thickness, the material gain at $N = 4 \times 10^{18}$ cm$^{-3}$ can marginally support the propagation of SPP-like modes around $\hbar\omega =$ 0.8 eV. However, the introduction of Au for ohmic contacts is expected to significantly increase the dissipation of SPP-like modes since Au is much more lossy than Ag. The gain margin is not sufficient in the presence of Au, and the dielectric is utilized to further reduce the loss.

### 4.2. *Insertion of dielectric layer*

To further lower the transparency gain of the SPP-like mode, we insert a TiO$_2$ dielectric layer beneath the Ag covering [27,28], namely, $d_2 \neq 0$ in Fig. 1. The resulted structure is still a slab WG. From section 4.1, if the upper WG cladding is composed of InP, and its thickness $d_3$ is smaller than 0.1 $\mu$m, the fundamental TE mode is efficiently cut off at $\hbar\omega = 0.8$ eV. In this section, the WG cladding would be composed of InP and TiO$_2$. The TE mode is still cut off under such circumstances, but modal features of the SPP-like mode are changed considerably. For related calculations, most of the length parameters are identical to those in the previous section. They are listed as follows: $d_3 = 0.1$ $\mu$m, $d_4 = 0.12$ $\mu$m, $d_5 = 0.4$ $\mu$m, and $d_1 = W_1 = \Lambda = 0$.

Figure 5(a) and (b) shows magnitude distributions of the electric field $|E_y(y)|$ and associated displacement field $|D_y(y)|$ of the SPP-like mode around the dielectric buffer layer with a thickness $d_2 = 0.04$ $\mu$m, respectively. The counterparts at $d_2 = 0.07$ $\mu$m are shown in Fig. 5(c) and (d). The photon energy $\hbar\omega$ is 0.8 eV. Both of the two profiles $|E_y(y)|$ in Fig. 5(a) and (c) exhibit high field strengths which are close to the Ag covering and are concentrated in respective dielectric buffer layers as a result of the continuity of $D_y(y)$. In a broad sense, these modes are

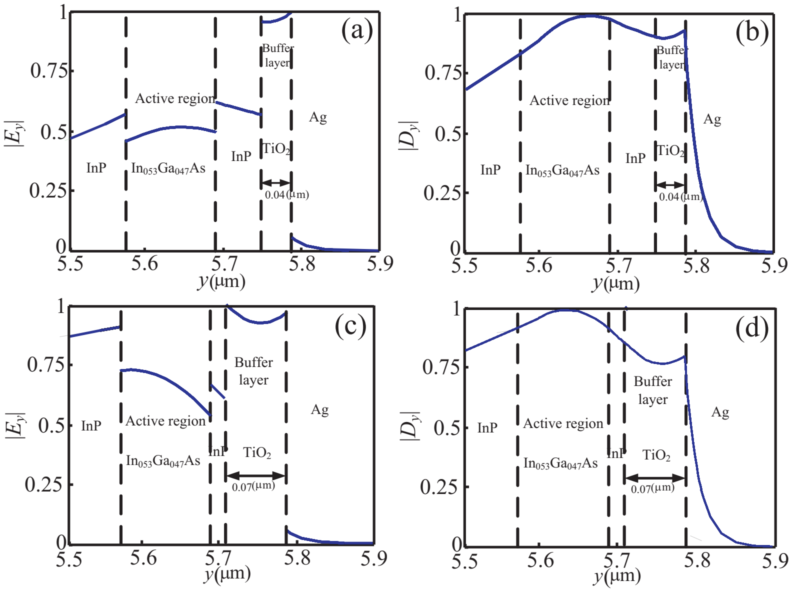

Fig. 5. The normalized magnitude distributions of $|E_y(y)|$ and $|D_y(y)|$ for the SPP-like mode in the presence of a dielectric buffer layer whose thickness $d_2$ is 0.04 $\mu$m [(a) and (b)] and 0.07 $\mu$m [(c) and (d)], respectively. The photon energy $\hbar\omega$ is 0.8 eV. The thick dielectric layer redistribute fields into the active region and lower WG cladding.

still SW-like. Nevertheless, the localized fields are not only consequences of metal-dielectric interfaces but also results of small dielectric buffers. The larger dielectric thickness $d_2$ usually lowers the portion of the optical field inside metals. However, the field is not necessarily drawn into the dielectric buffer. It may be redistributed into the active region and lower WG cladding if $d_2$ is sufficiently thick, as shown in Fig. 5(c).

Figure 6(a) shows the transparency gain $g_{\mathrm{tr},n}(\omega)$ at $\hbar\omega = 0.8$ eV as a function of thickness $d_3$ of the upper cladding layer for different dielectric heights $d_2 = 0.04$, 0.05, and 0.06 $\mu$m. These transparency gains are larger at the smaller $d_3$ since the active WG core is closer to the Ag covering. On the other hand, the larger $d_2$ results in the smaller transparency gains because the field strength is reduced in the metal and redistributed to the active region and lower WG cladding, as can be inferred from the field profiles in Fig. 5(c). The comparisons of transparency gain spectra $g_{\mathrm{tr},n}(\omega)$ with the material gain of $\mathrm{In}_{0.53}\mathrm{Ga}_{0.47}\mathrm{As}$ ($N = 4\times10^{18}$ cm$^{-3}$) at $d_3 = 0.1$ $\mu$m and $d_2 = 0.04$, 0.05, and 0.06 $\mu$m are shown in Fig. 6(b). The dielectric layer creates a significant gain margin for the SPP-like mode around the wavelength of 1.55 $\mu$m. This margin can be utilized to compensate the loss from Au contacts. On the other hand, we would not make the dielectric layer even thicker. As the openings below Au contacts act as current paths into the grating structure, the semiconductor InP below dielectric buffers plays the role of spreading the injection current into the active region. In views of an already thin cladding ($d_3 = 0.1$ $\mu$m), the excessive thickness $d_2$ of the dielectric layer could make the current distribution uneven. This factor should be kept in mind for designs of this grating laser.

### *4.3. Semiconductor laser with metal-dielectric grating*

For laser structures of the metal-dielectric grating, the period $\Lambda$ is set to 0.234 $\mu$m, which opens a photonic bandgap at the boundary $k_x = \pm\pi/\Lambda$ of the Brillouin zone (BZ). This period is

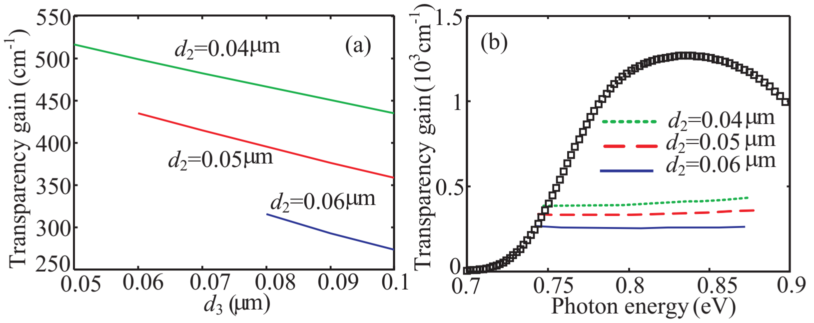

Fig. 6. (a) The transparency gains $g_{\text{tr},n}(\omega)$ of the SSP-like modes at $\hbar\omega = 0.8$ eV with buffer thicknesses $d_2 = 0.04$, 0.05, and 0.06 $\mu$m. The larger $d_2$ makes the transparency gain lower. (b) The transparency gain spectra at $d_2 = 0.04$, 0.05, and 0.06 $\mu$m. The cladding thickness $d_3$ is 0.1 $\mu$m. The gain spectrum at $N = 4\times10^{18}$ cm$^{-3}$ is shown in black squares. Considerable gain margins are present between the transparency gains and material one.

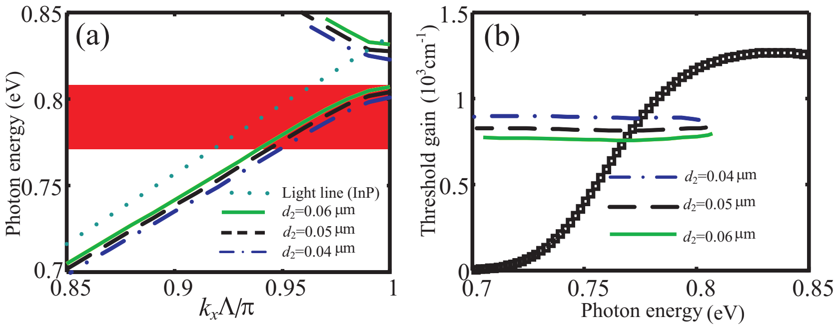

Fig. 7. (a) The dispersion relations $\hbar\omega_{n,k_x}$ of the three SPP-like modes at $W_1 = 0.7\Lambda$ and $d_2 = 0.04$, 0.05, and 0.06 $\mu$m. The three upper SPP branches become leaky modes once they cross the light line of InP (cyan dotted line). The red region marks the gain window of the lower SPP mode at $d_2 = 0.06$ $\mu$m. (b) Comparisons between the material gain at $N = 4\times10^{18}$ cm$^{-3}$ (black squares) and threshold gains $g'_{\text{th},n,k_x}$ of the three lower SPP branches in (a). The gain margins are smaller than their counterparts in Fig. 6(b)

chosen such that the bandedge of the SPP-like branch below the bandgap (lower SPP branch) is around $\hbar\omega$ =0.8 eV. We will examine the dispersion relation $\hbar\omega_{n,k_x}$ and threshold gain $g'_{\text{th},n,k_x}$ of the lower SPP branch by varying the thickness $d_2$ and width $W_1$ of the dielectric buffer. The SPP-like branch above the bandgap (upper SPP branch) only behaves like guided modes in a small $k_x$ space near the BZ boundary. As its frequency increases, the upper SPP branch crosses the light line of InP and is immersed into the continuum modes of the substrate. The corresponding radiation loss toward the InP substrate has a sudden and tremendous increment beyond this turning point, which can be told from the threshold gain $g'_{\text{th},n,k_x}$ of the upper SPP branch. Since the upper branch has a relatively small range of working frequencies, we should only focus on the lower branch.

The length parameters which are kept constant are listed as follows: $d_1 = 60$ nm (thickness of Au contacts), $d_3 = 0.1$ $\mu$m, $d_4 = 0.12$ $\mu$m, and $d_5 = 0.4$ $\mu$m.

Since the width $W_1$ of dielectric buffers is not identical to the period $\Lambda$, the current injection into the active region is made possible through InP regions below Au contacts. We first set

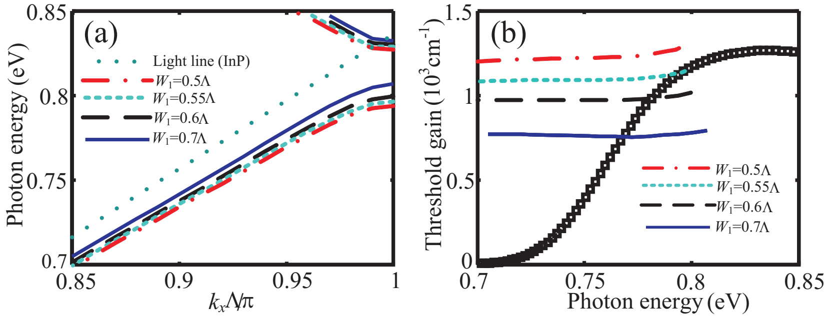

Fig. 8. (a) The dispersion relations $\hbar\omega_{n,k_x}$ at $d_2 = 0.06$ $\mu$m for $W_1 = 0.5$, 0.55, 0.6, and 0.7Λ. The smaller width $W_1$ makes dielectric buffers narrower and red shifts the dispersion relations. The light line of InP is shown as the cyan dotted line. (b) The threshold gains $g'_{\mathrm{th},n,k_x}$ of the lower SPP branches corresponding to the four widths $W_1$ in (a). The wider Au contacts at the smaller $W_1$ increase the threshold gain. Both the gain window and margin decrease accordingly. The material gain at $N = 4 \times 10^{18}$ cm$^{-3}$ is shown in black squares.

$W_1 = 0.7\Lambda$. The dispersion relations $\hbar\omega_{n,k_x}$ at $d_2 = 0.04$, 0.05, and 0.06 $\mu$m are shown in Fig. 7(a). Variations of the dielectric thickness change the photonic bandgap and slightly shift bandedges of the lower and upper SPP branches. The thicker dielectric buffer blue shifts the bandedge more. As a result, at $d_2 = 0.06$ $\mu$m, the upper branch is only guided (below the light line of InP) in quite limited ranges for both the wave number $k_x$ and frequency. For the lower SPP branches corresponding to three thicknesses $d_2$, their threshold gains $g'_{\mathrm{th},n,k_x}$ as a function of $\hbar\omega_{n,k_x}$ are shown in Fig. 7(b) up to the respective bandedges. The lower SPP branch with the largest thickness $d_2$ still exhibits the lowest threshold. However, the presence of Au contacts make all these threshold gains $g'_{\mathrm{th},n,k_x}$ significantly higher than the transparency gains $g_{\mathrm{tr},n}(\omega)$ of counterpart modes similar slab WGs [Fig. 6(b)]. For the lower SPP branch, its upper-bound photon energy of the gain window is the corresponding bandedge energy. On the other hand, the lower-bound photon energy marks the crossing between the threshold gain $g_{\mathrm{th},n,k_x}$ and material gain at $N = 4 \times 10^{18}$ cm$^{-3}$. The additional dissipation due to the proximity to Au contacts increases the threshold gain $g'_{\mathrm{th},n,k_x}$ and hence narrows the gain window. Meanwhile, the gain margin reserved for the compensation of the mirror loss is also reduced in the window. In Fig. 7(a), the gain window of the lower SPP branches at $d_2 = 0.06$ $\mu$m is shown in red. It covers an energy range of about 50 meV.

We further decrease the width $W_1$ of dielectric buffers to investigate its effect on the dispersion relation $\hbar\omega_{n,k_x}$ and threshold gain $g'_{\mathrm{th},n,k_x}$. The reduction of width $W_1$ has a similar effect to that due to the decrease of thickness $d_2$ on dispersion relations. Both of them make dielectric buffers smaller and therefore red shift the dispersion relation. In Fig. 8(a), the dispersion relations at $W_1 = 0.5$, 0.55, 0.6, and 0.7Λ indeed show this trend. Since the area of metal contacts become larger as the width $W_1$ of dielectric buffers turn smaller, the threshold gain $g'_{th,n,k_x}$ is enhanced accordingly by the extra loss from Au, as indicated in Fig. 8(b). Both the gain window and margin are reduced as $W_1$ decreases. From Fig. 8(b), as the width $W_1$ of dielectric buffers is reduced to 0.55Λ, the gain window and margin both vanish. In this case, the material gain at $N = 4 \times 10^{18}$ cm$^{-3}$ can only marginally support the propagation of SPP-like modes in a narrow frequency range, and there is no room for the compensation of the mirror loss at output facets. The reservation of this gain margin for the mirror loss is important for Bloch modes away from the bandedge. In those cases, the group velocity is on the order of the light speed in InP, and the round-trip time could be short in small laser cavities. This would enhance the loss rate at output

#222834 - $15.00 USD Received 11 Sep 2014; revised 23 Oct 2014; accepted 27 Oct 2014; published 3 Nov 2014

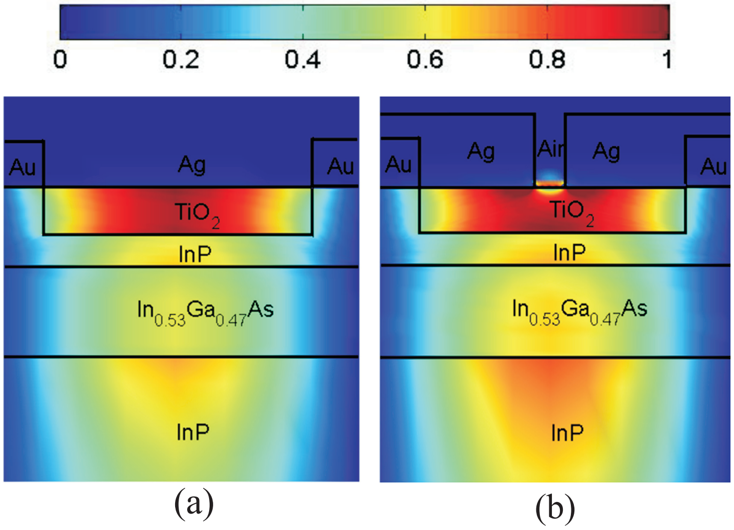

Fig. 9. Normalized field distributions $|E_y(\boldsymbol{\rho})|$ of (a) the lower SPP branch with the full Ag covering at the bandedge, and (b) the counterpart with a window which has a small width $W_2 = 0.1\Lambda \approx 23.4$ nm on the Ag covering. The thickness $d_2$ and width $W_1$ are 0.06 $\mu$m and $0.7\Lambda$, respectively. With the window, the surface field can reach the ambient environment for SW-enhanced applications of captured molecules and nanostructures.

facets. The effect has the less impact on bandedge modes due to their low group velocities. Since the gain margin is also large near the bandedge, bandedge modes would possibly lase first, which is also the case in typical SLs with distributed feedback structures.

The normalized field profile $|E_y(\boldsymbol{\rho})|$ of the bandedge mode ($\hbar\omega \approx 0.8$ eV) at $d_2 = 0.06$ $\mu$m and $W_1 = 0.7\Lambda$ is shown in Fig. 9(a). The design ensures that there are sufficient gain margin for the lasing action in this semiconductor grating structure at least at the benchmark carrier density $N = 4 \times 10^{18}$ cm$^{-3}$. On the other hand, the field inside the dielectric buffer would be blocked by the Ag covering with a thickness $d_5$ in tens of nanometers. It does not reach the ambient environment for SW-enhanced applications. Thinning the Ag covering below the optical penetration depth of about 12.5 nm could bring the field into the free space. However, the associated threshold gain $g_{\mathrm{th},n,k_x}$ significantly increases and is too large to achieve. To make SW-enhanced applications plausible, a small window with a width $W_2 = 0.1\Lambda \approx 23.4$ nm is opened at the center of the Ag covering ($d_5 = 85$ nm) to let out the surface field. The TE-like modes are still cut off in this condition. The resulted normalized field profile $|E_y(\boldsymbol{\rho})|$ at the bandedge is shown in Fig. 9(b). This window actually lowers the threshold gain of SPP-like modes slightly since the contact area with metal is reduced ($g'_{\mathrm{th},n,k_x} = 6.62 \times 10^2$ cm$^{-1}$). In this way, SW-enhanced measurements could be carried out on molecules or nanostructures captured into the window (target sizes smaller than $0.1\Lambda$). With the wider window, detections of the larger objects could also be possible.

## 5. Conclusion

We have presented the design of a SL based on the metal-dielectric grating which only supports SPP-like modes. The TE-like modes that are irrelevant for SW-enhanced applications are cut off through thickness variations of semiconductor-metal layer structures and insertions of dielectric buffers. In addition, the bulk semiconductor rather than specific nanostructures that favor TM-like modes is sufficient for the device scheme. We investigated the dispersion relation and threshold gain of the metal-dielectric grating. The structure was adjusted so that a sufficient gain margin remain for the lasing action of Bloch modes. With surface fields let out through thin windows opened on the metal surface, the laser structure could be utilized for SW-enhanced applications.

## Acknowledgments

This work is sponsored by Research Center for Applied Sciences, Academia Sinica, Taiwan, and Ministry of Science and Technology, Taiwan, under grant numbers NSC102-2221-E-001-027 and MOST103-2221-E-001-016.